Flexible quasi-solid-state sodium-ion capacitors developed using 2D metal-organic-framework array as reactor

Xu, Dongming; Chao, Dongliang; Wang, Huanwen; Gong, Yansheng; Wang, Rui; He, Beibei; Hu, Xianluo; Fan, Hong Jin

2018

https://hdl.handle.net/10356/105501

https://doi.org/10.1002/aenm.201702769

Article type: Full Paper

Flexible Quasi-Solid-State Sodium-Ion Capacitors Developed Using

Two-Dimensional Metal-Organic-Framework Array as Reactor

Dongming Xu, Dongliang Chao, Huanwen Wang*, Yansheng Gong, Rui Wang, Beibei He, Xianluo Hu*, Hong Jin Fan*

D.M. Xu, Prof. H. W. Wang, Prof. Y. S. Gong, Prof. R. Wang, Prof. B. B. He
Faculty of Material Science and Chemistry,
China University of Geosciences, Wuhan, 430074, China.
E-mail: wanghw@cug.edu.cn

Prof. X. L. Hu
State Key Laboratory of Materials Processing and Die & Mould Technology,
School of Materials Science and Engineering,
Huazhong University of Science and Technology, Wuhan 430074, China.
Email: huxl@mail.hust.edu.cn

Prof. H. W. Wang, Dr. D. L. Chao, Prof. H. J. Fan
School of Physical and Mathematical Sciences,
Nanyang Technological University,
Singapore 637371, Singapore.
Email: fanhj@ntu.edu.sg

Abstract:

Achieving high-performance Na-ion capacitors (NICs) has the particular challenge of matching both capacity and kinetics between the anode and cathode. Here we report a high-power NIC full device constructed from 2D metal-organic frameworks (MOFs) array as the reactive template. The MOF array is converted to N-doped mesoporous carbon nanosheets (mp-CNSs), which are then uniformly encapsulated with VO_2 and $Na_3V_2(PO_4)_3$ (NVP) nanoparticles as the electroactive materials. By this method, we are able to enhance significantly the high-power performance of the battery materials. It is discovered that such hybrid NVP@mp-CNSs array can render ultrahigh rate capability (up to 200 C, equivalent to discharge within 18 s) and superior cycle performance, which outperforms all NVP-based Na-ion battery cathode reported so far. We further assemble a quasi-solid-state flexible NIC based on the NVP@mp-CNSs cathode and the VO_2@mp-CNSs anode. This hybrid NIC device delivers both high energy density and power density as well as a good cycle stability (78% retention after 2000 cycles at 1 A g^{-1}). Our results demonstrate the powerfulness of MOF array as the reactor for fabricating electrode materials.

Introduction

With the rapid development of new-generation flexible electronics,[1, 2] such as wearable and portable electronic devices, roll-up displays, implantable biomedical products, conformable health-monitoring sensors, etc., future power sources are required to be mechanically flexible and also have both high energy and large power as well as long cycle life.[3-5] As the current main energy storage device, lithium ion batteries can provide high energy but usually suffer from a low power rate and short life span. To overcome these drawbacks, researchers propose the so-called metal-ion capacitors, or hybrid batteries, which combine a battery anode and a capacitor electrode in order to achieve trade-off between conventional battery and supercapacitor.[6-8] It is expected that such hybrid system delivers a capacitor-like fast charge/discharge rate and battery-like high capacity. Since the first introduction in 2001, great

progress has been achieved in the field of hybrid lithium-ion capacitors (LICs) through better understanding of the charge storage mechanism and the development of high-performance nanostructured materials. In a LIC, the capacitive cathode is typically a carbonaceous material that enables fast charge−discharge processes, while the reported battery-type anode includes $Li_4Ti_5O_{12}$,[9, 10] graphite,[11] TiO_2,[12] MnO[13] and $LiVO_3$.[14]

Sodium-ion batteries are becoming one of most promising battery technologies for the foreseeable grid-scale applications, because of more earth-abundant sodium source and their similar chemistry to that of the existing lithium-ion batteries.[15-22] Despite the potential low-cost, constructing hybrid sodium ion capacitors (NICs) faces more challenge because most Na host materials have a rather sluggish kinetic due to the large Na ion sizes. Research on NICs began in early 2012,[23] and was focused on improving the power capability of the anode in order to match the fast kinetics of the capacitive cathode. Strategies to increase sodium ion (Na^+) and electron (e^-) transport kinetics of NIC electrodes reported so far include: 1) *developing new electrode materials* (such as 2D MXene Ti_2C,[24] V_2C),[25] 2) *constructing more conductive electrode structures by hybridizing with carbon* (such as $NaTi_2(PO_4)_3$/rGO,[26] C@NVP,[27] Nb_2O_5@C/rGO,[28] TiO_2 mesocages@rGO,[29] and 3) *shortening the ion diffusion and electron transport lengths by rational designing nanostructures* (such as TiO_2 nanospheres,[30] Ti(O,N) nanowires,[31] $Na_2Ti_3O_7$ nanosheets[32]). Despite these efforts, these reported anodes of NIC still have relatively limited rate performance and especially low Na-ion storage capacity. Among other reasons, most of these electrode materials are powder samples, which require substantial amount of conductive additives (such as Super P, 10~20 wt%) and binder in order to make compact films. This not only weakens the electron transport but also unable to meet the flexibility requirement.

As for the cathode, the most widely used cathode material in NICs is commercial activated carbon (AC). AC has a rather low capacitance (30~60 mAh g^{-1}) particularly at high discharge currents, because of the limited ion transport kinetics within the ultrasmall sized (typically <0.5 nm) channels.[33] This results in a low energy utilization for NICs according to the capacity

equation ($1/C_{\text{NIC}} = 1/C_{\text{cathode}} + 1/C_{\text{anode}}$). Although MXene V$_2$C [25] and Na$_2Fe_2$(SO$_4$)$_3$ [24] have been used as cathodes to improve the energy density of NICs, fabrication of a flexible cathode with supercapacitor-like power performance and battery-like capacity for hybrid NICs still remains a challenge.

Based on the above considerations, the key to a high-performance NIC is to match the high-rate capability between anode and cathode by properly tailoring the nanostructure and achieving superb ion/electron conductivity. In this work, we design and fabricate a N-doped mesoporous carbon nanosheet array on flexible substrates by using metal-organic frameworks (MOFs) array as the reactive template. The interconnected Co/Zn MOF nanosheets anchored onto flexible carbon fiber cloth surfaces (CFC) are first converted into ordered arrays of mesoporous carbon nanosheets (mp-CNSs). Such a mesoporous carbon sheet network with oxygen/nitrogen-containing functional groups allows anchoring of metal ions by the complexation or electrostatic interactions. In order to develop a high-power NIC device, we deposit VO$_2$ and NVP to form interconnected VO$_2$@mp-CNSs/CFC and NVP@mp-CNSs/CFC materials, which can be directly used as electrodes without any conductive additives or binders. In these hybrid electrodes, VO$_2$ or NVP nanoparticles are also enwrapped by highly graphitic carbon shells within the mp-CNSs scaffold. This unique electrode design delivers multiple advantages: 1) *suppress the aggregation of electroactive nanoparticles*, 2) *accommodate the volume change during the cycle processes*, 3) *maintain a high electrical and ionic conductivity of the overall electrode*, and 4) *give rise to robust flexibility.* As a consequence, the VO$_2$@mp-CNSs/CFC electrode is demonstrated to have the pseudocapacitive characteristic of Na-ion storage, while the battery-type NVP cathode also exhibits ultrahigh rate charge/discharge property equivalent to graphene-based supercapacitors. Finally, by utilizing both flexible VO$_2$@mp-CNSs/CFC as anode, NVP@mp-CNSs/CFC as cathode, and a sodium ion conducting gel polymer as the electrolyte, we obtained quasi-solid-state hybrid Na-ion capacitors. This hybrid NIC device can deliver a high energy density (~161 Wh kg^{-1} and 8.83 mWh cm^{-3}) and a

high power density (24 kW kg^{-1} and 1.32 Wh cm^{-3}) that outperform nearly all previous hybrid devices.
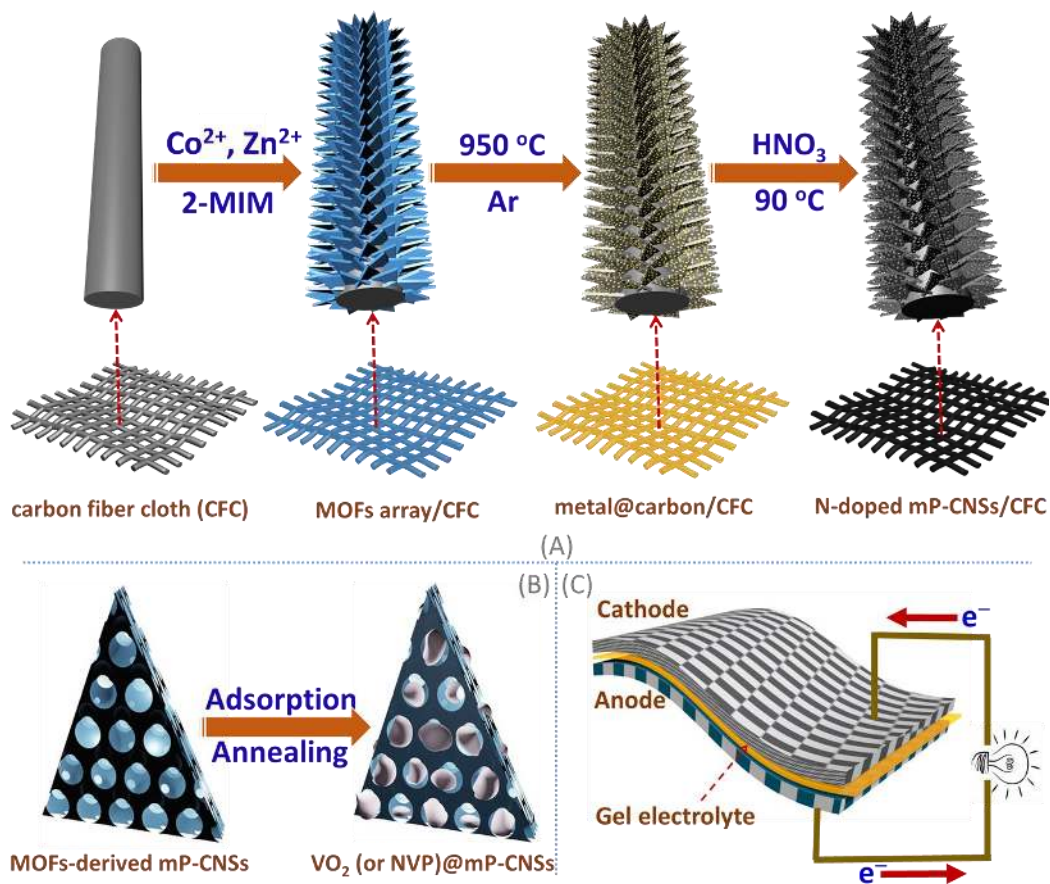
Results and Discussion

Figure 1 Synthetic route for cathode and anode materials and the full Na-ion capacitor device. Schematic illustration of (A) arrays of nitrogen-doped mesoporous graphitic carbon nanosheets (mp-CNSs) derived from 2D MOFs array on carbon fiber cloth, (B) VO$_2$@ mp-CNSs (and NVP@mp-CNSs) by depositing VO$_2$ (and NVP) on the mp-CNSs array. (C) A flexible quasi-solid-state sodium-ion capacitor containing a cathode and an anode made from NVP@mp-CNSs and VO$_2$@ mp-CNSs, respectively.

2D MOF-Derived Mesoporous Carbon Nanosheet (mp-CNS) Arrays

The formation process of the mp-CNSs/CFC involves three major steps as shown

schematically in **Figure 1**. In the *first* step, an oxygen plasma treatment makes the surface of carbon fiber cloth hydrophilic, which is the key to a successful growth of ordered Co/Zn MOFs arrays (see experimental section for more details). The FESEM images shows that MOF nanosheets are uniformly grown on the carbon fibers forming an interconnected 3D network but without destroying the ordered woven structure of the pristine CFC (see **Figure 2A**, **D** in main text and S1 in Supporting Information). The homogeneous deposition of MOFs on the CFC can also be indicated by the uniform color change from pristine black to purple (Figure S2 in Supporting Information). The average thickness of MOF nanosheets is 150 nm (**Figure 2A**). We found that this Co/Zn-based MOFs can be deposited also on other substrates, such as nickel foam, celgard 2400 separator, and graphene oxide paper (Figure S3 in Supporting Information). In the *second* step, under argon atmosphere at 950 °C, in situ and confined carburization reaction converts the obtained MOFs into metal cobalt/carbon nanosheet arrays on CFC. During the carbonization process of organic ligands, the metal cobalt ions in MOFs can not only be reduced as catalysts to promote high degree of graphitization, but also act as template, which are uniformly incorporated into carbon matrix due to the atomic level dispersion in MOF precursor. Moreover, organic ligands "2-methylimidazole (2-MIM)" contain nitrogen species, which can form *in-situ* nitrogen-doping in carbon after annealing. As shown in **Figure 2E**, there is no agglomeration and coalescence in the resultant metal/N-doped carbon/CFC sample and the uniform nanosheet array structure can still be retained. The metal nanoparticles (10−50 nm) are uniformly anchored into the cross-linked carbon nanosheets (**Figure 2B**, S1D in Supporting Information). *Finally*, the annealed sample was dipped in HNO$_3$ aqueous solution at 90 ºC for 24 h to remove the metal nanoparticles, generating a substantial amount of mesopores within the carbon nanosheets. The resultant N-doped mp-CNSs/CFC can be folded and rolled up (Figure S4 in Supporting Information), which reveals its flexible feature. Furthermore, these MOF-derived carbon nanosheets have a strong adhesion to the carbon cloth substrates; the mp-CNSs/CFC does not change morphology after ultrasonication (200 W for 30 min).
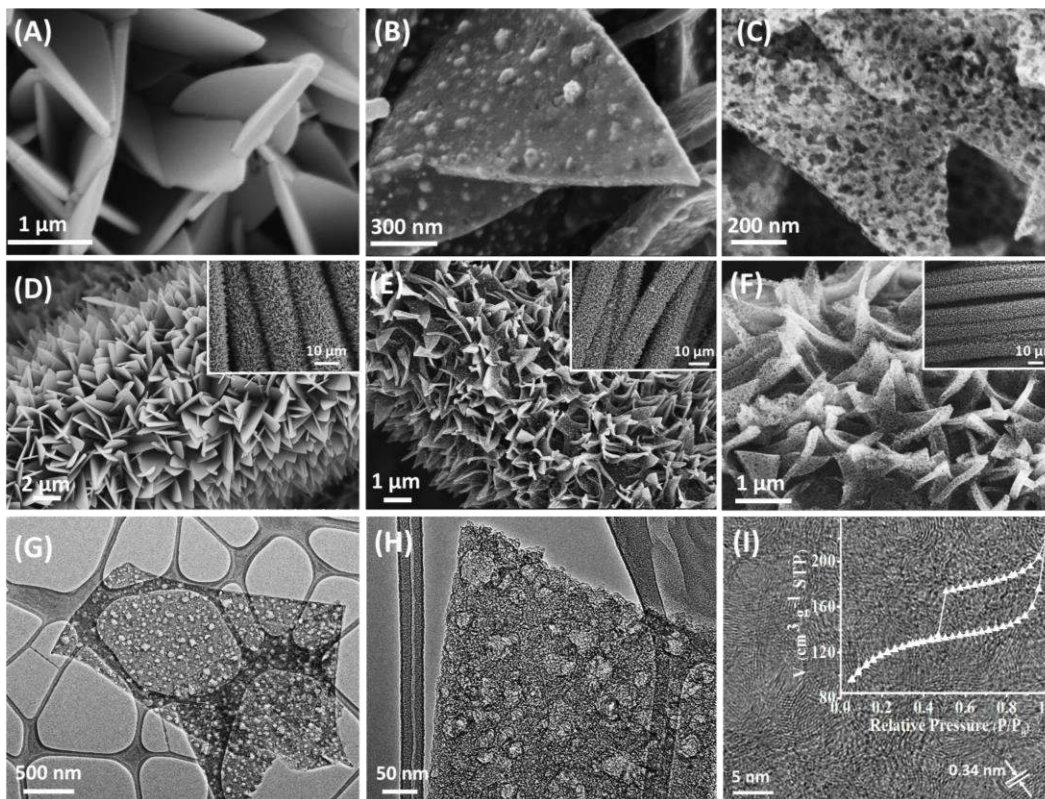
Figure 2 MOF arrays and its conversion to mp-CNSs. FESEM images of Co/Zn MOFs array on CFC (A, D), metal cobalt@carbon/CFC (B, E), nitrogen-doped mp-CNSs (C, F), and TEM images (G-I) of MOFs-derived mp-CNSs. Inset of Figure 2I is Nitrogen adsorption and desorption isotherm of nitrogen-doped mp-CNSs derived from Co/Zn MOFs.

The microstructure of the as-synthesized mp-CNSs/CFC was further investigated by electron microscopes. The carbon nanosheets have an average thickness of ~100 and contain well-defined mesopores of ~20 nm in size, as seen from both high-resolution FESEM and TEM images (**Figure 2F, G and H**). High-resolution TEM (HRTEM) image reveals that the mesopore walls consist of localized graphitic structures (see **Figure 2I**), where the fringes with lattice spacing of 0.34 nm correspond to the graphitic (002) plane. Such a high graphitization is beneficial to improving the electric conductivity.[12]

The conversion process from MOFs precursor to mesoporous carbon and its graphitic structure were further confirmed using XRD, Raman spectroscopy, N$_2$ adsorption-desorption analysis, and XPS measurements. Data and detailed analysis are presented in Supporting

Information (Figure S5-9, Supporting Information). Here we only state major findings. The characteristic graphitic XRD peak of our MOFs-derived mp-CNSs is much sharper than that of commercial activated carbon, which implies the graphitic crystalline structure. In addition, the presence of the 2D Raman peak at ~2684 cm^{-1} is remarkable and strongly indicates high graphitization in our MOFs-derived CNSs,[34, 35] in agreement with the XRD and TEM results. From the nitrogen adsorption and desorption spectrum, the distinct hysteresis loop in the range of 0.7~1.0 *P/P$_o$* (inset of **Figure 2I**) suggests the presence of an appreciable amount of mesopores (corresponding to a surface area of 387.8 m^2 g^{-1}). Such a mesoporosity originates from the removal of metal templates during the rearrangement of carbon slices. All these characterizations unravel the mesoporous structure, uniform N-doping, high degree of graphitization within our mp-CNSs arrays.

Based on this highly conductive, porous, and flexible mp-CNSs/CFC as both current collector and 3D scaffold, we then grow electroactive materials on top of it. As typical Na-ion battery materials, VO$_2$ and Na super-ionic conductor (NASICON)-type NVP were selected for the anode and cathode, respectively (**Figure 1**). The detailed synthesis procedure is presented in the experimental section. We note that the obtained electrodes, VO$_2$@mp-CNSs/CFC and NVP@mp-CNSs/CFC, are still fully bendable without breaking, and completely preserve the 3D interconnected array structure. In the following, we will discuss their structural properties and electrochemistry separately.

Flexible Anode Material: VO$_2$@mp-CNSs/CFC

The VO$_2$@mp-CNSs/CFC electrode was fabricated by a simple adsorption-annealing process. Well-dispersed VO$_2$ tiny nanoparticles were achieved by using the *in-plane* mesopore template. During the adsorption process, V$_2$O$_5$ is firstly converted to soluble [VO(O$_2$)(OH$_2$)$_3$]$^+$, [VO$_2$]$^+$ and then to VO(OH)$_3$.[36, 37]
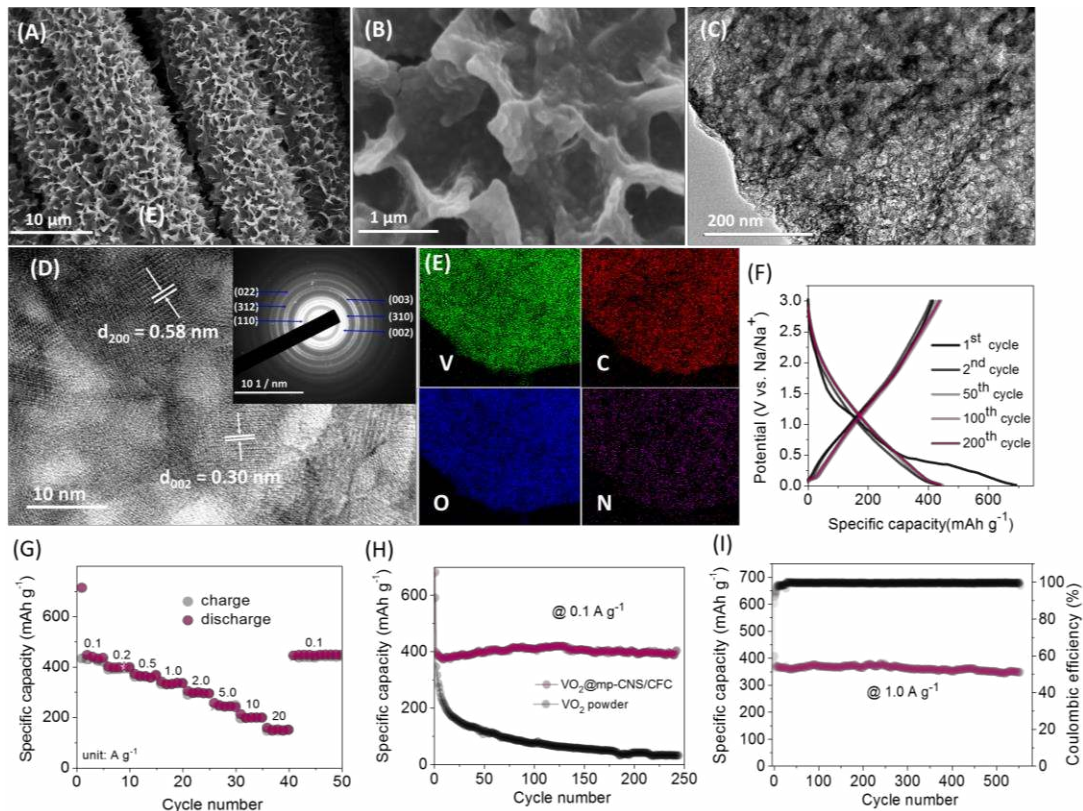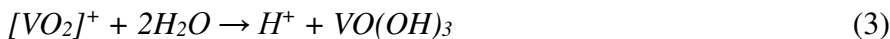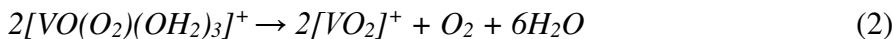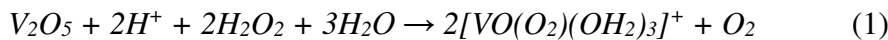
Figure 3 Structure and electrochemistry of VO₂@mp-CNSs. FESEM (A, B), TEM (C, D), SAED pattern (inset of Figure 3D), and EDS mapping results (E) of VO₂@mp-CNSs. Electrochemical properties of the VO₂@mp-CNSs/CFC electrode in a Na half-cell between 0.01 and 3 V vs. Na: (F) The typical charging/discharging curves at a current density of 0.1 A g^{-1}. (G) Rate performance at different current densities. (H) Cycling performance of the VO₂@mp-CNSs/CFC and pure VO₂ at 0.1 A g^{-1}. (I) Cycling performance of the VO₂@mp-CNSs/CFC electrode at a high current density of 1 A g^{-1}.

$$V_2O_5 + 2H^+ + 2H_2O_2 + 3H_2O \rightarrow 2[VO(O_2)(OH_2)_3]^+ + O_2 \qquad (1)$$

$$2[VO(O_2)(OH_2)_3]^+ \rightarrow 2[VO_2]^+ + O_2 + 6H_2O \qquad (2)$$

$$[VO_2]^+ + 2H_2O \rightarrow H^+ + VO(OH)_3 \qquad (3)$$

After the annealing process, VO(OH)₃ is further reduced to VO₂ on mp-CNSs/CFC.

$$2VO(OH)_3 + H_2 \rightarrow 2VO_2 + 4H_2O \qquad (4)$$

One can easily see that VO₂ nanoclusters are uniformly dispersed on the CFC without aggregation (**Figure 3A and B**). The ultrafine nanoparticles with the size of ~5 nm are interconnected with each other. The voids between the clusters (**Figure 3C-D**) provide ample

active sites for Na-storage and offer sufficient contacts with the electrolyte. The lattice spacing of 0.58 and 0.30 nm corresponds to the (200) and (002) crystal planes of VO_2, respectively, as seen from the HRTEM image (**Figure 3D**). The selected area electron diffraction (SAED) pattern demonstrates a polycrystalline structure of the VO_2 nanocrystals. All the rings in SAED can be uniquely indexed in the space group $C_{2/m}$ with standard lattice constants a = 12.03 Å, b = 3.693 Å, and c = 6.42 Å (β = 106.6°) for VO_2(B) with a monoclinic structure (JCPDS no. 31−1438). The elemental mapping analysis confirms the coexistence and the homogenous dispersion of V, C, O and N elements within the nanosheet framework (**Figure 3E**).

We now investigate the sodium storage performance of the VO_2@mp-CNSs/CFC electrode. The galvanostatic charge–discharge (GCD) curves in the potential window of 0.005–3 V (vs Na/Na$^+$) are presented in **Figure 3F**. These GCD curves show no obvious charge/discharge plateaus during the sodium intercalation process ($VO_2 + xNa^+ + xe^- \leftrightarrow Na_xVO_2$).[36] The GCD curves did not change significantly after the first cycle. The first discharge and charge capacities are 692 and 443 mAh g^{-1}, respectively, corresponding to a Coulombic efficiency of 64%. The first irreversible capacity loss is generally ascribed to the formation of solid electrolyte interphase (SEI) layer. The 5th-cycle capacities calculated from the GCD discharge curves (Figure S10 in Supporting Information) suggest that the VO_2@mp-CNSs/CFC electrode has an excellent capability retention when the current density changes from 0.1 to 20 A g^{-1} (**Figure 3G**). In contrast, the pure VO_2 powder electrode has a poor rate capability and cycle stability. And the pure mp-CNSs/CFC electrode shows very small capacity around 50 mAh g^{-1} at 1.0 A g^{-1} (Figure S11-13 in Supporting Information).

The VO_2@mp-CNSs/CFC electrode also shows an excellent long-cycle stability. We observed no obvious capacity losses for the VO_2@mp-CNSs/CFC electrode over 250 cycles at a rate of 0.1 A g^{-1} (**Figure 3H**). However, under the same mass loading with the VO_2@mp-CNSs/CFC electrode, the specific capacity of the VO_2 powder electrode sharply decreases from the initial 345 mAh g^{-1} to only 26 mAh g^{-1} at 250th cycle under the same current density. This demonstrates clearly the key advantage of our 3D VO_2@mp-CNSs/CFC electrode.

The same test was carried out at a much higher current density of 1 A g^{-1} (after five-cycle activation at 0.2 A g^{-1}), a high capacity of 352 mA h g^{-1} can be obtained even over 550 cycles, with an overall capacity decay as low as 4% (**Figure 3I**). After 550 cycles at 1 A g^{-1}, the electrode was examined by FESEM. It is revealed that the original 3D interconnected array morphology is well preserved (Figure S14 in Supporting Information), demonstrating a high structural stability under fast discharge/charge cycles for long lifespan Na$^+$ storage.

VO$_2$ has been reported as an intercalation-type battery material that exhibits dominating pseudocapacitive feature.[36, 37] To quantify this, we conducted kinetics analysis to explain the above superior sodium-storage performance of the VO$_2$@mp-CNSs/CFC electrode. As shown in Figure S15 in the Supporting Information, from 1 to 100 mV s^{-1}, a good linear relationship can be observed between logarithm cathodic peak current and logarithm scan rate with $R^2 = 0.99851$. The kinetic analysis also allows us to approximately distinguish the fraction of the current from surface capacitance and that from Na$^+$ semi-infinite linear diffusion.[38, 39] For example, it is found that about 78% of the total current of the electrode is contributed by the capacitive mechanism at the sweep rate of 10 mV s^{-1}. This result is in accordance with the electrochemistry result, namely, non-obvious redox peaks in CV curves and quasi-linear discharge curves. It suggests that the Na$^+$ storage mechanism of the VO$_2$@mp-CNSs/CFC electrode is mainly pseudocapacitive in nature during the charge/discharge process. Such high Na-ion storage capacity, excellent rate/cycling stabilities, as well as suitable voltage range, of the VO$_2$@mp-CNSs/CFC make it an excellent anode candidate for hybrid NICs.

Flexible Cathode Material: NVP@mp-CNSs/CFC

To overcome the capacity limit of the traditional double layer carbon cathode, here we use Na super-ionic conductor (NASICON)-type NVP to increase the energy density of NICs. However, NVP has an intrinsically low electronic conductivity due to its crystal structure, and thus the theoretical capacity is not fully accessible especially at high power rates. Considering the multiple advantages of our MOFs-derived mp-CNSs/CFC in comparison with other carbon
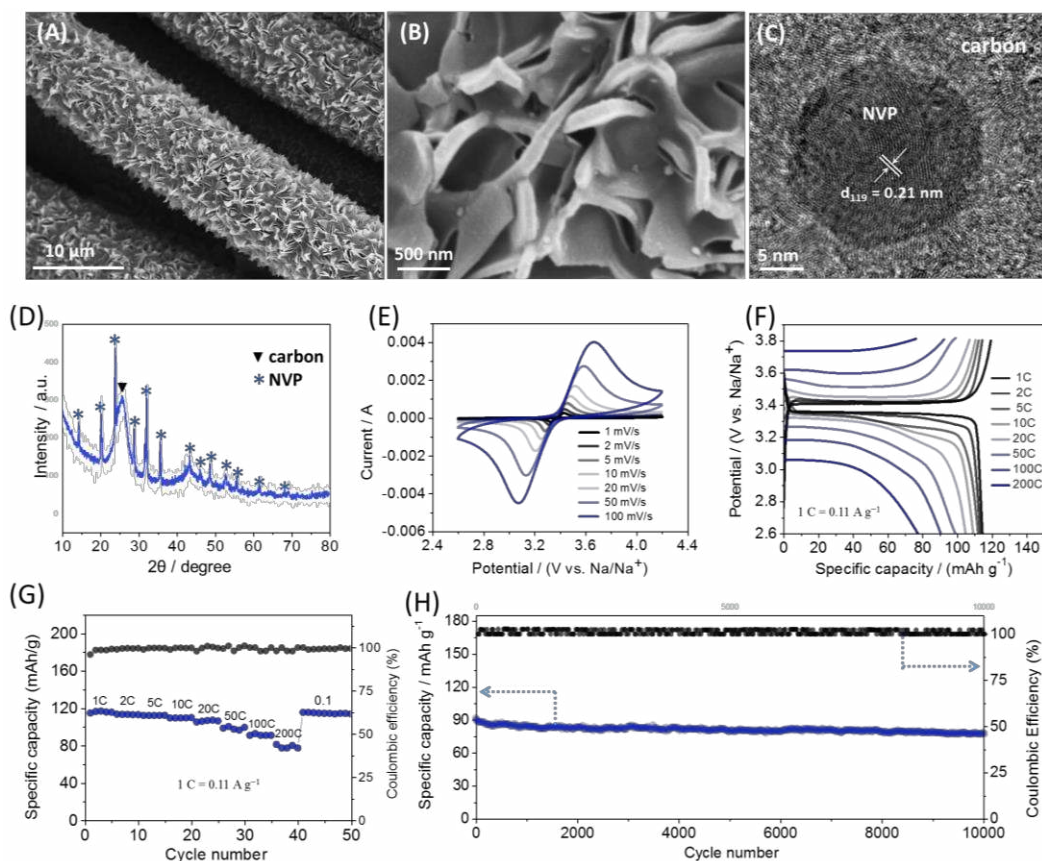
Figure 4 Structure and electrochemistry of NVP@mp-CNSs. (A, B) FESEM, (C) TEM, (D) XRD pattern, (E) CV curves at various scan rates from 1 to 100 mV s^{-1}, (F) Charging/discharging curves, (G) Rate performance at different current densities and (H) cycling performance at 100 C of the NVP@mp-CNSs sample.

materials, it is worthwhile exploiting the possibility of uniform coating NVP onto the surfaces of mp-CNSs for achieving superior rate capability and stable capacities (details of synthesis are in the experimental section). Similar to the VO$_2$@mp-CNSs, the pristine mp-CNSs array is fully covered with NVP nanoparticles (**Figure 4A, 4B**). Such hierarchically geometric configuration allows easy electrolyte penetration and suppresses the agglomeration of NVP nanoparticles during the electrochemical reaction process, thereby improving the activity and stability of the electrode. As shown in **Figure 4C**, one NVP nanoparticle with the size of ~20 nm is embedded within graphitic carbon matrix (**Figure 4C**), which endows the composite with high electronic conductivity. Clear lattice fringes are observed in which the 0.21 nm interfringe spacing

corresponds to the (119) interplane of rhombohedral NVP. The composition of the NVP@mp-CNSs product is confirmed by XRD data (Figure 4D); Apart from the peaks of the CFC substrate, all the diffraction peaks can be indexed to a rhombohedral $Na_3V_2(PO_4)_3$ phase with the space group of R3c (JCPDS card No. 62–0345).[40, 41]

To investigate the electrochemical performance of the NVP@mp-CNSs electrode, we first prepared half-cells using coin cell with sodium metal as the counter and reference electrodes. **Figure 4E** displays the CV curves in the voltage window of 2.6–4.2 V versus Na^+/Na at various scan rates from 1 to 100 mV s^{-1}. A pair of well-defined redox peaks are observed, which corresponds to the V^{3+}/V^{4+} redox couple with two sodium extraction/insertion,[42, 43] i.e., $Na_3V_2(PO_4)_3 \leftrightarrow NaV_2(PO_4)_3 + 2Na^+ + 2e^-$. Importantly, even at an ultrahigh scan rate of 100 mV s^{-1}, the CV curve retains a similar shape, indicating the fast diffusion of sodium ions into the NVP@mp-CNSs network. The GCD profiles of NVP@mp-CNSs at various current densities also clearly demonstrate the high rate capability (**Figure 4F**). The specific capacity is quite close to the theoretical capacity (117 mAh g^{-1}) not only at 1 C; but even at 50 C, one still has 109 mAh g^{-1} (Here 1C means that the full capacity is discharged or charged in 1 h, corresponding to 0.11 A g^{-1}). At an ultrahigh rate of 200 C (within a full discharge in 18 s), the electrode can still deliver a specific capacity of 82 mAh g^{-1}, which is about 70% of its theoretical capacity (**Figure 4G**). This NVP@mp-CNSs electrode also exhibits an outstanding capacity stability. After 300 cycles at 1 C, the reversible capacity can still retain 95% of initial value (Figure S16, Supporting Information). Most importantly, the electrode can display an ultralong cycling life for 10,000 cycles under an ultrahigh rate of 100 C (**Figure 4H**). The specific capacity is about 81 mA h g^{-1} after 10 000 cycles, corresponding to capacity retention of 87%. The above high-rate and long cycling quality of our NVP@mp-CNSs electrode are comparable or superior to the best results reported for NVP-based electrodes in the literature (see detailed comparison in Table S1 Supporting Information). Therefore, with this mesoporous carbon scaffold, we are able to endow a battery material with super high-rate capability that is necessary for its NIC application.

Flexible Quasi-Solid-State Hybrid Sodium-Ion Capacitor

Taking account of the outstanding sodium ion storage characteristics and robustness of both the pseudocapacitive VO$_2$@mp-CNSs/CFC and battery-type NVP@mp-CNSs/CFC electrodes, we now construct a flexible quasi-solid-state sodium ion capacitor using the sodium ion conducting gel polymer as the electrolyte. Shown in **Figure 5A** is a schematic illustration of the charge storage mechanism of the NIC full cell. During the charging process, the VO$_2$@mp-CNSs/CFC anode undergoes reversible Na$^+$ insertion whereas the NVP@mp-CNSs cathode involves Na$^+$ removal. The above reactions are reversed during the discharging process. **Figure 5B** shows SEM images of the prepared P(VDF-HFP) membrane which is highly porous with the average pore size about 2 μm. When the P(VDF-HFP) membrane was dipped into the NaClO$_4$/PC/FEC(5%) solution, the color of the membrane changed from white to transparent, indicating the organic electrolyte successfully entrapped into the pores of the P(VDF-HFP) matrix (Figure S17A-B, Supporting Information). This gel polymer electrolyte can also be easily bent and folded without breaking. More detailed information of the P(VDF-HFP) membrane is presented in Figure S17, Supporting Information.

Figure 5C shows the GCD curves for the as-assembled flexible NIC measured at different current densities (based on the total weight of the anode and cathode materials) in the potential range of 1.0~3.8 V. These GCD curves are quasi-linear, different from that of NVP@mp-CNSs. At a low current density of 0.1 A g^{-1}, the NIC can deliver a reversible capacity of 86 mAh g^{-1} (Figure 5D), which is much higher that of the reported Ti$_2$CT$_x$//alluaudite Na$_2$Fe$_2$(SO$_4$)$_3$ NIC (26.6 mAh g^{-1}).[24] Even at an ultrahigh current density of 20 A g^{-1} (higher than most reported NICs, usually <5 A g^{-1}), the specific capacity of 27 mAh g^{-1} is still achieved. Our NIC full cell has no evident structural failure and nearly identical discharge curves after bending to 90$^{\rm o}$ (**Figure 5E**). After repeated bending for 50 times at ~90$^{\rm o}$, it can be found that the specific capacity is not obviously sacrificed (>95% retention), demonstrating its excellent mechanical flexibility and stability. Furthermore, the NIC shows stable cyclability over 2000 cycles with the capacity retention of 78% at a current density of 1 A g^{-1} (**Figure 5F**). The Coulombic efficiency

for cycling at 1 A g^{-1} reaches 99.7% after a few initial cycles. In contrast to half cells that show stable cycling performance with no obvious decay, the NIC device has some capacity decay, which may be due to partial loss of active Na$^+$ during the cycling process. Even so, such a high sodium-ion storage performance for this flexible quasi-solid-state NIC, to our knowledge, has never been reached before (Table 2, Supporting Information).
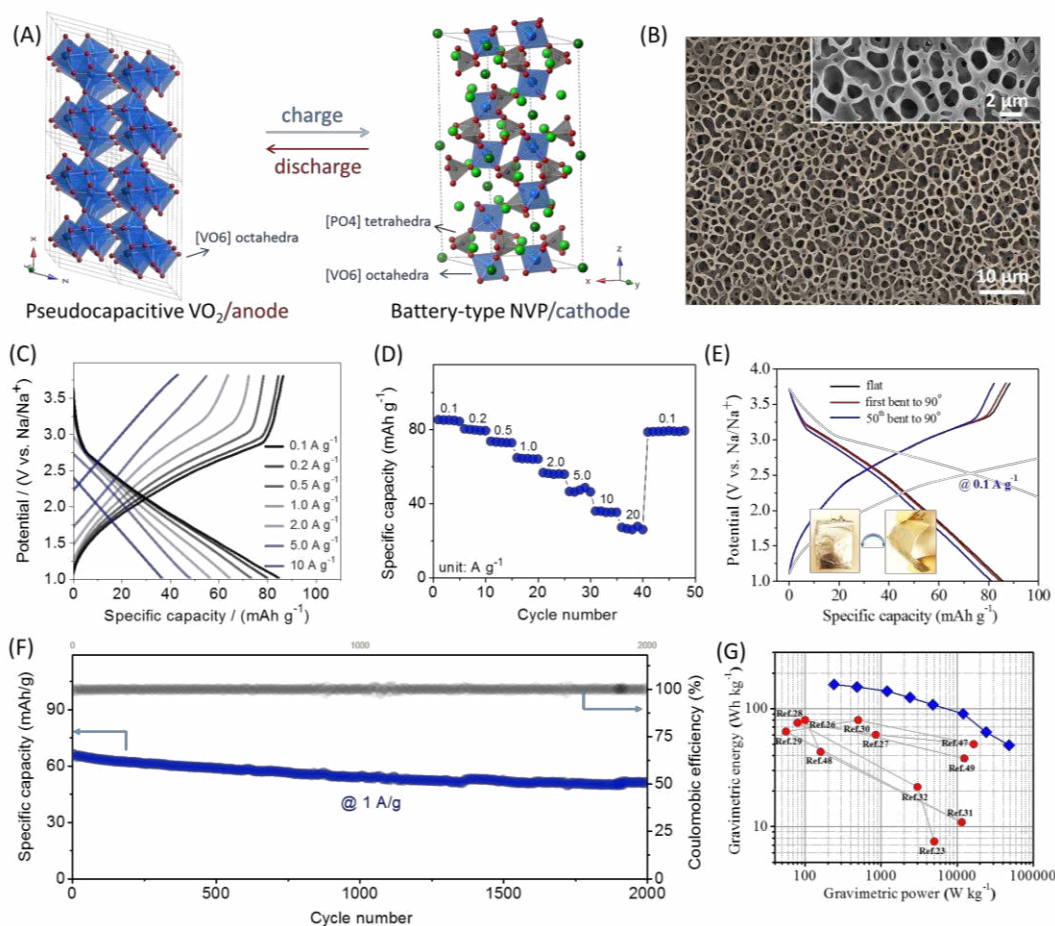

Figure 5 Na-ion capacitor (NIC) full device. (A) Schematic illustration of the NIC device using flexible NVP@mp-CNSs/CFC and VO$_2$@mp-CNSs/CFC electrodes as cathode and anode. (B) SEM images of the P(VDF-HFP) membrane (porous gel polymer). (C) Charging/discharging curves and (D) Rate performance of the as-assembled NIC at different current densities based on the total mass of NVP@mp-CNSs and VO$_2$@mp-CNSs. (E) The charge-discharge curves of the quasi-solid-state NIC device under flat and bent (90°) status (shown as inset). (F) Cycling performance at 1 A g^{-1} and (G) Ragone plots of the flexible quasi-solid-state NIC.

The Ragone plot (energy density vs power density) of the VO$_2$@mp-CNSs/CFC//NVP@mp-CNSs/CFC NIC device is shown in **Figure 5G**. The energy density and power density values are calculated by integrating galvanostatic discharge curves and using the total mass of the two electrodes. Our NIC can achieve a high energy density of 161 Wh kg^{-1} at a power density of 240 W kg^{-1}. Even at an extremely high power density of 48 kW kg^{-1}, the NIC can still deliver 49 Wh kg^{-1}. Here the power density of 48 kW kg^{-1} means a full charge–discharge within 9.6 s. Note that typical power densities for supercapacitors are in the range of 1–20 kW kg^{-1} but with energy densities not exceeding 1~20 Wh kg^{-1}.[8, 44] Obviously, our MOFs-derived carbon array-based NIC combines the advantages of batteries and supercapacitors, and hence, is of a great potential to be applied as high power and high energy systems. The energy densities of the present quasi-solid-state NIC device are considerably higher than those values of the state-of-the-art reported NICs [23, 26-32, 45-47] (Table 2, Supporting Information) and other energy storage systems such as lithium ion capacitors,[48-50] aqueous asymmetric SCs,[51, 52] ionic liquid-based SCs [33, 53] and Ni/Fe batteries[54, 55]. The corresponding volumetric energy and power densities are shown in Figure S18, Supporting Information, in which the flexible quasi-solid NIC device achieves a high volumetric energy density of 8.8 mWh cm^{-3} and power density of 1.32 W cm^{-3}. Those values are much higher than those in the recently reported flexible energy storage devices, such as H-TiO$_2$@MnO$_2$//H-TiO$_2$@C device (0.30 mWh cm^{-3}, 0.23 W cm^{-3}),[56] Na$_2$Ti$_3$O$_7$//rGO NIC (1.30 mWh cm^{-3}, 0.07 W cm^{-3}),[32] T-Fe$_2$O$_3$/PPy//MnO$_2$ supercapacitor (1.30 mWh cm^{-3}, 0.07 W cm^{-3}).[57]

In order for a metal-ion capacitor to perform with both high energy and high power, it is essential to enable fast-rate capability to battery electrode materials. Our flexible quasi-solid-state NIC benefits to their surface microstructure and high electronic conductivity of both anode and cathode. Specifically,

First, VO$_2$ (and NVP) nanocrystals are encapsulated in N-doped graphitic mesoporous carbon nanosheets by chemical bonding which ensures structural integrity during repeated Na-ion insertion/extraction. FTIR spectra were used to investigate the mutual interaction in the hybrid

structure. As shown in **Figure 6C**, the bands appearing at 1208 and 1572 cm^{-1} in mp-CNSs correspond to the C–N stretching peak and the skeletal vibration of graphitic carbon, respectively. For the VO$_2$@mp-CNSs and NVP@mp-CNSs, the characteristic absorption peak of graphitic carbon at ~1572 cm^{-1} can be clearly observed, which is consistent with mp-CNSs. However, the C–N stretching peak for VO$_2$@mp-CNSs (1226 cm^{-1}) and NVP@mp-CNSs (1226 cm^{-1}) exhibits an obvious red-shift as compared to that of mp-CNSs (1208 cm^{-1}). This red-shift phenomenon reveals the coupling interaction between electronegative nitrogen (N) in mp-CNSs and d^3 orbital of V in VO$_2$ or NVP, which is also supported by the XPS results (see Figure S19 and discussion, Supporting Information). This implies an intimate integration of mp-CNSs to VO$_2$ or NVP.
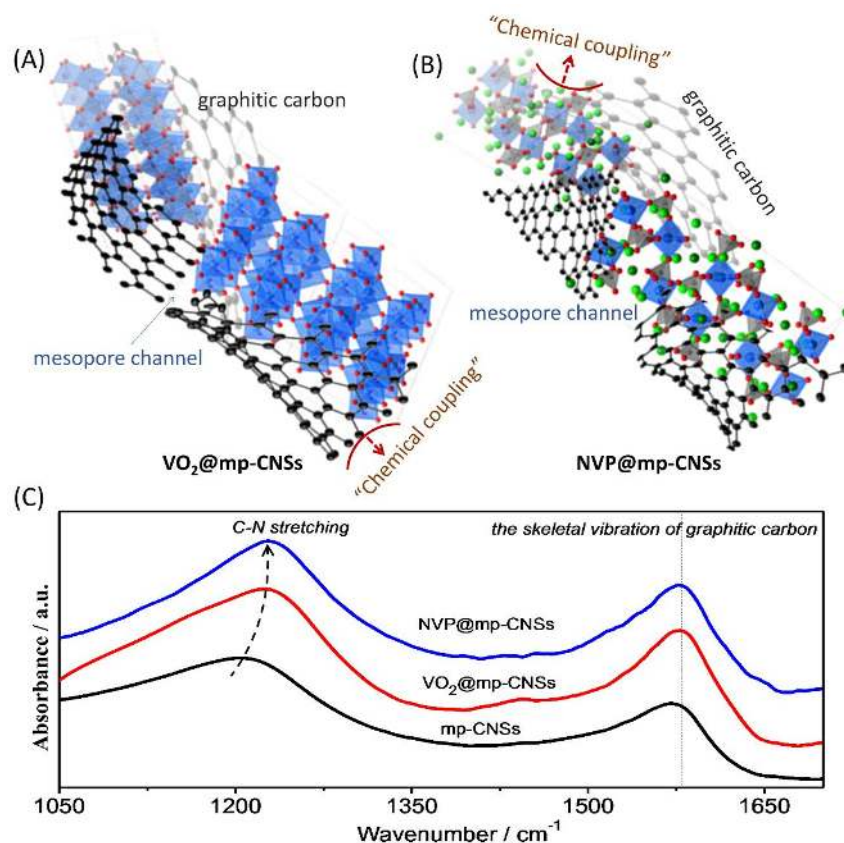

Figure 6 Schematic illustration of high-rate Na$^+$ storage of the (A) NVP@mp-CNSs/CFC and (B) the VO$_2$@mp-CNSs/CFC. (C) FTIR spectra of the three samples.

Second, 2D MOF-derived carbon nanosheets exhibit *high degree of graphitization*, which

17

ensures excellent electronic conductivity through the hybrid network (Figure S20, Supporting Information). The *abundant in-plane mesopores* provide a highly conductive pathway for sodium ions. This makes our mp-CNSs better than the vertical graphene nanosheets grown by PECVD on carbon fibers, where the later has nearly no porosity.

Finally, as for the NIC structure, the super high-rate NVP cathode not only overcomes the small capacity of the traditional double layer carbon cathode, but also matches the supercapacitive VO_2 anode in order to achieve high power of the whole device. In fact, our design concept can be versatile given the fact that many Na-ion battery materials exhibit pseudocapacitive feature by tailoring the nanostructure and/or crystal phase.

Conclusion

We have developed an effective MOF-derived synthesis approach to prepare Na-ion capacitors that deliver both high energy and power (energy density of 161 Wh kg^{-1} at a power density of 240 W kg^{-1}, based on the total weight of the two electrodes). Large-area arrays of nitrogen-doped mesoporous carbon nanosheets on carbon fiber cloth (mp-CNSs/CFC) are successfully fabricated via pyrolysis of 2D Co/Zn-MOFs arrays on CFC. The as-prepared mp-CNSs/CFC offers an electronically and ionically conducting 3D continuous network for electroactive particles encapsulation. Based on this platform, we choose VO_2 (pseudocapacitive material) and NVP (typical sodium-ion battery cathode material) as the respective anode and cathode materials, and encapsulate them uniformly within the mesoporous carbon. Because of the high surface areas, high conductivity and N-doping of the mp-CNSs, the obtained quasi-solid-state NIC device delivers high power densities up to 48 kW kg^{-1} (the corresponding energy density is still nearly 50 Wh kg^{-1}). This result overcomes the trade-off limit associated with conventional hybrid batteries. This is the first report of flexible quasi-solid-state sodium-ion capacitor with high energy and power densities. This is just one demonstration, but we believe that, by exploiting the compositional and structural versatility of 2D MOF array, one can

construct many more high-performance electrodes for not only hybrid metal-ion capacitors and fast-rate batteries, but also electrocatalysts.

Experimental

Materials and Reagents: $Co(NO_3)_2 \cdot 6H_2O$ (≥98%), $Zn(NO_3)_2 \cdot 6H_2O$ (98%), 2-methylimidazole (99%), V_2O_5 (≥98%), $H_2C_2O_4$ (98%), H_2O_2 (30 wt. % in H_2O), $NaCO_3$ (99%) and $NH_4H_2PO_4$ (≥98%) were obtained from Sigma-Aldrich and were used as received without further purifications. Solvents of analytical grade were used as received.

Synthesis of Co/Zn MOFs nanosheets/carbon fiber cloth: Before growth of MOFs, the carbon fiber cloth (CFC) substrates were firstly cleaned by sonication sequentially in acetone, deionized (DI) water, and ethanol for 30 min each. After then, the cleaned CFC was further treated with oxygen plasma using a March PX-250 plasma etching system (100 sccm oxygen gas flow, 70 mTorr, and 100 W power density for 20 min). In a typical process, 2 mmol of $Co(NO_3)_2 \cdot 6H_2O$ and 1 mmol of $Zn(NO_3)_2 \cdot 6H_2O$ were dissolved in 100 mL deionized water, termed A. 20 mmol of 2-MIM was dissolved in another 100 mL deionized water, termed B. After 60 min magnetic stirring at room temperature, the solution A was quickly poured into the solution B and a piece of the above CFC (6×8 cm²) was placed in the mixing solution. Being kept still for 2 h, Co/Zn MOFs/CFC was washed successively with water and ethanol and then dried at 60 °C under vacuum overnight. For comparison, Co MOFs/CFC was also synthesized by the same procedure as the Co/Zn MOFs/CFC by replacing 1 mmol of $Zn(NO_3)_2 \cdot 6H_2O$ with 1 mmol of $Co(NO_3)_2 \cdot 6H_2O$.

Synthesis of arrays of mesoporous nitrogen-doped carbon nanosheets/carbon fiber cloth (mp-CNSs/CFC): The as-prepared Co/Zn MOFs/CFC was annealed at 950 °C for 6 h with a heating rate of 1 °C min⁻¹ under argon atmosphere. After cooling down, the sample was dipped in 6 M HNO_3 at 100 °C for 24 h. Then, the obtained sample (mp-CNSs/CFC) was dried at 60 °C for 24 h under vacuum overnight.

Synthesis of VO₂@mp-CNSs/CFC and NVP@mp-CNSs/CFC: 1.5 mmol of V_2O_5 and 5 mmol of $H_2C_2O_4$ were dissolved in 10 mL of distilled water at 75 °C until a dark blue solution was formed. Then 2 mL of 30% H_2O_2 and 20 mL of ethanol were added and continuously stirred for ~30 min. The mp-CNSs/CFC was dipped into the above solution for 24 h and was then freeze-dried overnight. Finally, the mp-CNSs/CFC with the VO_2 precursor was

annealed at 450 ℃ in Ar + H$_2$ (5%) for 2 h to obtain VO$_2$@mp-CNSs/CFC.

5 mmol of V$_2$O$_5$ and 2 mL of 30% H$_2$O$_2$ was added into 20 mL of distilled water under vigorous stirring to give a yellow solution. Following, 15 mmol of NaCO$_3$ and 15 mmol NH$_4$H$_2$PO$_4$ were sequentially dissolved into mixed solution under stirring ~30 min. Subsequently, the mp-CNSs/CFC was dipped into the above solution for 24 h and was freeze-dried overnight. Finally, the mp-CNSs/CFC with the NVP precursor was annealed at 800 ℃ in Ar + H$_2$ (5%) for 6 h to obtain NVP@mp-CNSs/CFC.

Synthesis of sodium ion conducting gel polymer: The porous P(VDF-HFP) membrane was prepared according to literature reported by Wu's group with minor modifications.[58] Typically, the P(VDF-HFP) powder was dissolved into a mixture of DMF and distilled water at 80 °C with a weight ratio of polymer: DMF: H$_2$O=15:85:3. The solution was cast onto a glass plate, and then dipped into a water bath at 80 °C, which formed a porous white membrane. The white membrane was dried under vacuum at 90 °C for 24 h. Finally, the dried P(VDF-HFP) membrane was cut into circular pieces. Finally, these membranes were soaked in an organic electrolyte (1 mol L^{-1} NaClO$_4$ solution in dissolved in propylene carbonate with 5 vol% fluorinated ethylene carbonate) over 12 h in a glove box to obtain the gel polymer electrolyte.

Material characterization: The samples were characterized using XRD (RigakuD/Max-2550 with Cu-Ka radiation), Nitrogen adsorption/desorption isotherms at 77 K (ASAP Tri-star II 3020 model), SEM (JEOL, Model JSM-7600F), TEM (JEOL, Model JEM-2100), Micro-Raman spectroscopy (LabRAM HR Raman Instrument, incident wavelength is 514.4 nm, 50x objective lens). The XPS measurements were performed by a VG ESCALAB 220i-XL system using a monochromatic Al Ka1 source (1,486.6eV). FTIR spectra were recorded at 0.5 cm^{-1} resolution on a Bruker Vertex 70 V with 0.1 cm^{-1} accuracy using a three-refection attenuated total refection (ATR) accessory with a ZnSe internal refection element.

Electrochemical measurement: Standard CR2032-type coin cells were assembled in an argon-filled glove box (Mbraun, Germany) with the as-fabricated VO$_2$@mp-CNSs/CFC and NVP@mp-CNSs/CFC as the working electrode (without any binder or additives). Half-cell configurations were assembled using Na-metal foil as counter and reference electrodes, and sodium ion conducting gel polymer as the electrolyte. Hybrid LICs were fabricated with NVP@mp-CNSs/CFC as the cathode material and VO$_2$@mp-CNSs/CFC as the anode material under the optimized mass loadings (~1 × 1 cm^2; VO$_2$@mp-CNSs mass: ~1 mg, NVP@mp-CNSs mass: ~2.5 mg). The

NVP@mp-CNSs/CFC and the VO$_2$@mp-CNSs/CFC electrodes were pressed together with a Na$^+$ conducting gel polymer as both electrolyte and separator. The ion conductivity was tested by electrochemical impedance spectroscopy (EIS), which was performed from 1 to 100 Hz with the voltage amplitude of 5 mV at open circuit potential. Specifically, the cell configuration for ionic conductivity tests was "the sandwich structure", in which one piece of the P(VDF-HPF) GPE film (see Figure S17B), one spacer, and one wave spring were sealed in a 2032 coin cell in a glove box. The ionic conductivity was calculated using Equation: $\sigma = L/RA$, where L, R and A were the film thickness, the resistance and the geometric area of the film, respectively.

Supporting Information
((Supporting Information is available online from Wiley InterScience or from the author)).

References and Notes

[1]   J. A. Rogers, T. Someya, Y. Huang, *Science* **2010**, *327*, 1603.

[2]   L. Peng, Y. Zhu, H. Li, G. Yu, *Small* **2016**, *12*, 6183.

[3]   X. Wang, X. Lu, B. Liu, D. Chen, Y. Tong, G. Shen, *Adv. Mater.* **2014**, *26*, 4763.

[4]   N. Li, Z. Chen, W. Ren, F. Li, H.-M. Cheng, *Proc. Natl. Acad. Sci. U. S. A.* **2012**, *109*, 17360.

[5]   D. Chao, C. Zhu, P. Yang, X. Xia, J. Liu, J. Wang, X. Fan, S. V. Savilov, J. Lin, H. J. Fan, Z. X. Shen, *Nat. Commun.* **2016**, *7*, 12122.

[6]   F. Zhang, T. Zhang, X. Yang, L. Zhang, K. Leng, Y. Huang, Y. Chen, *Energy Environ. Sci.* **2013**, *6*, 1623.

[7]   E. Lim, H. Kim, C. Jo, J. Chun, K. Ku, S. Kim, H. I. Lee, I.-S. Nam, S. Yoon, K. Kang, J. Lee, *ACS Nano* **2014**, *8*, 8968.

[8]   Y. Wang, Y. Song, Y. Xia, *Chem. Soc. Rev.* **2016**, *45*, 5925.

[9]   V. Aravindan, D. Mhamane, W. C. Ling, S. Ogale, S. Madhavi, *ChemSusChem* **2013**, *6*, 2240.

[10] H.-G. Jung, N. Venugopal, B. Scrosati, Y.-K. Sun, *J. Power Sources* **2013**, *221*, 266.

[11] S. R. Sivakkumar, A. G. Pandolfo, *Electrochim. Acta* **2012**, *65*, 280.

[12] H. Wang, H. Yi, C. Zhu, X. Wang, H. J. Fan, *Nano Energy* **2015**, *13*, 658.

[13] H. Wang, Z. Xu, Z. Li, K. Cui, J. Ding, A. Kohandehghan, X. Tan, B. Zahiri, B. C. Olsen, C. M. Holt, D. Mitlin, *Nano Lett.* **2014**, *14*, 1987.

[14] L. Shen, S. Chen, J. Maier, Y. Yu, *Adv. Mater.* **2017**, *29*.

[15] H. Li, L. Peng, Y. Zhu, D. Chen, X. Zhang, G. Yu, *Energy Environ. Sci.* **2016**, *9*, 3399.

[16] H. Li, Y. Ding, H. Ha, Y. Shi, L. Peng, X. Zhang, C. J. Ellison, G. Yu, *Adv Mater* **2017**, *29*, 1700898.

[17] D. Chen, L. Peng, Y. Yuan, Y. Zhu, Z. Fang, C. Yan, G. Chen, R. Shahbazian-Yassar, J. Lu, K. Amine, G. Yu, *Nano Lett* **2017**, *17*, 3907.

[18] L. Peng, P. Xiong, L. Ma, Y. Yuan, Y. Zhu, D. Chen, X. Luo, J. Lu, K. Amine, G. Yu, *Nat Commun* **2017**, *8*, 15139.

[19] L. Peng, Y. Zhu, D. Chen, R. S. Ruoff, G. Yu, *Adv. Energy Mater.* **2016**, n/a.

[20] H. Li, L. Peng, Y. Zhu, X. Zhang, G. Yu, *Nano Lett* **2016**, *16*, 5938.

[21] F. Wang, X. Wang, Z. Chang, X. Wu, X. Liu, L. Fu, Y. Zhu, Y. Wu, W. Huang, *Adv Mater* **2015**, *27*, 6962.

[22] D. Chao, P. Liang, Z. Chen, L. Bai, H. Shen, X. Liu, X. Xia, Y. Zhao, S. V. Savilov, J. Lin, Z. X. Shen, *ACS Nano* **2016**, *10*, 10211.

[23] Z. Chen, V. Augustyn, X. Jia, Q. Xiao, B. Dunn, Y. Lu, *ACS Nano* **2012**, *6*, 4319.

[24] X. Wang, S. Kajiyama, H. Iinuma, E. Hosono, S. Oro, I. Moriguchi, M. Okubo, A. Yamada, *Nat. Commun.* **2015**, *6*, 6544.

[25] Y. Dall'Agnese, P. L. Taberna, Y. Gogotsi, P. Simon, *J Phys Chem Lett* **2015**, *6*, 2305.

[26] R. Thangavel, B. Moorthy, D. K. Kim, Y.-S. Lee, *Adv. Energy Mater.* **2017**, *7*, 1602654.

[27] R. Thangavel, K. Kaliyappan, K. Kang, X. Sun, Y.-S. Lee, *Adv. Energy Mater.* **2016**, *6*, 1502199.

[28] E. Lim, C. Jo, M. S. Kim, M.-H. Kim, J. Chun, H. Kim, J. Park, K. C. Roh, K. Kang, S. Yoon, J. Lee, *Adv. Funct. Mater.* **2016**, *26*, 3711.

[29] Z. Le, F. Liu, P. Nie, X. Li, X. Liu, Z. Bian, G. Chen, H. B. Wu, Y. Lu, *ACS Nano* **2017**, *11*, 2952.

[30] S. Liu, Z. Cai, J. Zhou, A. Pan, S. Liang, *J. Mater. Chem. A* **2016**, *4*, 18278.

[31] J. Dong, Y. Jiang, Q. Li, Q. Wei, W. Yang, S. Tan, X. Xu, Q. An, L. Mai, *J. Mater. Chem. A* **2017**, *5*, 10827.

[32] S. Dong, L. Shen, H. Li, G. Pang, H. Dou, X. Zhang, *Adv. Funct. Mater.* **2016**, *26*, 3703.

[33] C. Liu, Z. Yu, D. Neff, A. Zhamu, B. Z. Jang, *Nano Lett.* **2010**, *10*, 4863.

[34] Z. Chen, W. Ren, L. Gao, B. Liu, S. Pei, H. M. Cheng, *Nat. Mater.* **2011**, *10*, 424.

[35] H. Wang, Y. Zhang, W. Sun, H. T. Tan, J. B. Franklin, Y. Guo, H. Fan, M. Ulaganathan, X.-L. Wu, Z.-Z. Luo, S. Madhavi, Q. Yan, *J. Power Sources* **2016**, *307*, 17.

[36] D. Chao, C. Zhu, X. Xia, J. Liu, X. Zhang, J. Wang, P. Liang, J. Lin, H. Zhang, Z. X. Shen, H. J. Fan, *Nano Lett.* **2015**, *15*, 565.

[37] X. Xia, D. Chao, C. F. Ng, J. Lin, Z. Fan, H. Zhang, Z. X. Shen, H. J. Fan, *Mater. Horiz.* **2015**, *2*, 237.

[38] H. S. Kim, J. B. Cook, H. Lin, J. S. Ko, S. H. Tolbert, V. Ozolins, B. Dunn, *Nat. Mater.* **2017**, *16*, 454.

[39] P. Simon, Y. Gogotsi, B. Dunn, *Science* **2014**, *343*, 1210.

[40] C. Zhu, K. Song, P. A. van Aken, J. Maier, Y. Yu, *Nano Lett.* **2014**, *14*, 2175.

[41] X. Rui, W. Sun, C. Wu, Y. Yu, Q. Yan, *Adv. Mater.* **2015**, *27*, 6670.

[42] C. Zhu, P. Kopold, P. A. van Aken, J. Maier, Y. Yu, *Adv. Mater.* **2016**, *28*, 2409.

[43] W. Zhang, Y. Liu, C. Chen, Z. Li, Y. Huang, X. Hu, *Small* **2015**, *11*, 3822.

[44] X.-L. Wu, L.-Y. Jiang, F.-F. Cao, Y.-G. Guo, L.-J. Wan, *Adv. Mater.* **2009**, *21*, 2710.

[45] J. Ding, H. Wang, Z. Li, K. Cui, D. Karpuzov, X. Tan, A. Kohandehghan, D. Mitlin, *Energy Environ. Sci.* **2015**,

8, 941.

[46] H. Li, Y. Zhu, S. Dong, L. Shen, Z. Chen, X. Zhang, G. Yu, *Chem. Mater.* **2016**, *28*, 5753.

[47] Y.-E. Zhu, L. Yang, J. Sheng, Y. Chen, H. Gu, J. Wei, Z. Zhou, *Adv. Energy Mater.* **2017**, 1701222.

[48] W. Zuo, R. Li, C. Zhou, Y. Li, J. Xia, J. Liu, *Adv. Sci.* **2017**, *4*, 1600539.

[49] H. Wang, Y. Zhang, H. Ang, Y. Zhang, H. T. Tan, Y. Zhang, Y. Guo, J. B. Franklin, X. L. Wu, M. Srinivasan, H. J. Fan, Q. Yan, *Adv. Funct. Mater.* **2016**, *26*, 3082.

[50] V. Aravindan, J. Gnanaraj, Y. S. Lee, S. Madhavi, *Chem. Rev.* **2014**, *114*, 11619.

[51] H. B. Li, M. H. Yu, F. X. Wang, P. Liu, Y. Liang, J. Xiao, C. X. Wang, Y. X. Tong, G. W. Yang, *Nat. Commun.* **2013**, *4*, 1894.

[52] B. G. Choi, M. Yang, W. H. Hong, J. W. Choi, Y. S. Huh, *ACS Nano* **2012**, *6*, 4020.

[53] Y. Li, Z. Li, P. K. Shen, *Adv. Mater.* **2013**, *25*, 2474.

[54] H. Wang, Y. Liang, M. Gong, Y. Li, W. Chang, T. Mefford, J. Zhou, J. Wang, T. Regier, F. Wei, H. Dai, *Nat. Commun.* **2012**, *3*, 917.

[55] C. Guan, W. Zhao, Y. Hu, Q. Ke, X. Li, H. Zhang, J. Wang, *Adv. Energy Mater.* **2016**, *6*, 1601034.

[56] X. Lu, M. Yu, G. Wang, T. Zhai, S. Xie, Y. Ling, Y. Tong, Y. Li, *Adv. Mater.* **2013**, *25*, 267.

[57] L. Wang, H. Yang, X. Liu, R. Zeng, M. Li, Y. Huang, X. Hu, *Angew. Chem. Int. Ed.* **2017**, *56*, 1105.

[58] Y. Q. Yang, Z. Chang, M. X. Li, X. W. Wang, Y. P. Wu, *Solid State Ionics* **2015**, *269*, 1.